Bifurcation Generated Mechanical Frequency Comb

David A. Czaplewski, Changyao Chen, Daniel Lopez, Oriel Shoshani, Axel M. Eriksson, Scott Strachan, and Steven W. Shaw

Phys. Rev. Lett. **121**, 244302 — Published 14 December 2018

DOI: 10.1103/PhysRevLett.121.244302

Bifurcation Generated Mechanical Frequency Comb

David A. Czaplewski,* Changyao Chen, and Daniel Lopez
Center for Nanoscale Materials, Argonne National Laboratory, Lemont, IL, 60439, USA

Oriel Shoshani
Ben-Gurion University of the Negev, Beer-sheva 84105, Israel

Axel M. Eriksson
Chalmers University of Technology, SE-412 96 Göteborg, Sweden

Scott Strachan
SiTime, Santa Clara, CA, 95054, USA

Steven W. Shaw
Florida Institute of Technology, Melbourne, FL, 32901, USA
(Dated: October 22, 2018)

We demonstrate a novel response of a nonlinear micromechanical resonator when operated in a region of strong, non-linear mode coupling. The system is excited with a single drive signal and its response is characterized by periodic amplitude modulations that occur at timescales based on system parameters. The periodic amplitude modulations of the resonator are a consequence of nonlinear mode coupling and are responsible for the emergence of a "frequency comb" regime in the spectral response. By considering a generic model for a 1:3 internal resonance, we demonstrate that the novel behavior results from a saddle node on an invariant circle (SNIC) bifurcation. The ability to control the operating parameters of the micromechanical structures reported here, makes the simple micromechanical resonator an ideal testbed to study the dynamic response of SNIC behavior demonstrated in mechanical, optical and biological systems.

Mode coupling has led to many novel and interesting effects whose applications span across mechanical [1] [2] [3] [4], optical [5] [6] [7], quantum information [8] [9] [10] [11] and biological [12] [13] domains. It has been observed in mechanical systems with dimensions in the nanoscale [1] [14] [15] [16], microscale [17] [18] and in macroscale objects like the Tacoma Narrows Bridge [19]. Typically, mode coupling is achieved by parametric excitation where the coupled modes do not have a rational frequency relationship. As a consequence, this non-resonant modal coupling is inherently inefficient due to the mismatch in frequencies between modes [9]. Alternatively, resonant mode coupling capitalizes on the condition where the resonant frequencies of the distinct modes satisfy a commensurate relationship enabling strong coupling and efficient energy transfer among them. Resonant mode coupling has been used to improve frequency stability of non-linear resonators [20], to coherently exchange mechanical energy between modes [21], and for frequency conversion [22].

In recent years, mode coupling in micro-mechanical devices has been used to demonstrate the generation of "frequency combs", a series of equally spaced discrete spectral lines [10] [16] [23] [24] [18] [25] [26] [27]. The generation of the combs in these systems results from parametric mixing between frequencies in mechanical systems displaying both linear and non-linear responses typically requiring multiple external drive signals and/or coupling between three or more modes. In this Letter, we use a single nonlinear mechanical resonator driven by a single actuation signal to generate a frequency comb. We observe bursting behavior in the dynamic response of the microelectromechanical (MEMS) resonator and the corresponding generation of a frequency comb with time scales five orders of magnitude different than the resonant frequency. The vastly different timescales between the mechanical response and the bursting behavior along with the periodic modulations in amplitude indicates a significantly different mechanism for frequency comb generation than the ones reported above. To gain understanding of this new behavior, we introduce the normal form describing the motion of the resonator, show the creation of a saddle node on an invariant circle (SNIC) bifurcation, and for the first time, characterize the effect of the SNIC bifurcation on a mechanical structure. Additionally, we determine system parameters from the experimental measurements and show agreement between theory and experimental data. Finally, control of the bursting behavior is demonstrated experimentally through variation of the system parameters resulting in a tunable frequency-comb spacing in good agreement with theory. Furthermore, the bursting behavior demonstrated here represents a universal response for any type of system that follows the normal form with similar system parameters.

The electromechanical resonators used in this study

are clamped-clamped single crystal silicon beams with lateral comb drives for electrical actuation of the device and sensing of its motion through a displacement current (Fig. 1a) [20] [21] [28]. The resonator is driven with amplitude, $V_{\rm o}$, at frequency, $f_{\rm F}$. The two vibrational modes of interest are the fundamental in-plane flexural mode with a natural frequency of 62973 Hz and a linear decay rate of $\Gamma_{\rm flex}$= 1.9 Hz, and a torsional mode with natural frequency of 192960 Hz and a linear decay rate, $\Gamma_{\rm tor}$= 4.7 Hz (see supplemental materials for further information).

It is the dynamical interaction of the in-plane flexural mode and the out-of-plane torsional mode which results in the generation of a frequency comb in these nonlinear resonators. When the flexural mode is driven with sufficient amplitude ($V_{\rm o} > 300\mu V$), the mode exhibits frequency stiffening due to its Duffing non-linearity [29] [30] (Fig. 1b). In the nonlinear regime of operation, the resonator is bistable and can follow two different stable responses: a large amplitude (upper) branch and a small amplitude (lower) branch. When increasing the drive frequency, the resonator follows the upper branch until a critical frequency, $f_{\rm SN}$. At $f_{\rm SN}$, the high amplitude branch (represented by a node in the rotating frame) merges with an unstable branch (a saddle in the rotating frame) and the two annihilate one another. As a consequence, the resonator drops to the lower branch, shown by the vertical lines in Fig. 1b. As the drive strength and frequency are successively increased, the operation point approaches a 1:3 internal resonance with the torsional mode. In the vicinity of the internal resonance ($f_{\rm F} \approx f_{\rm tor}/3$), the system undergoes a saddle node (SN) bifurcation, which occurs before the expected Duffing SN as a result of the nonlinear mode coupling [20].

For sufficiently large drive amplitude at the internal resonance, the response of the resonator does not transition to the lower branch at the SN, but exhibits complex periodic modulations as shown in Fig. 1c. The timescale of these modulations is approximately 5 orders of magnitude longer than the drive period, $1/f_{\rm F}$. From Fig. 1c, we see that the first (flexural) and third (torsional) signals exhibit fluctuations with distinct transitions from calmer epochs to periods of large modulations; generating a comb in the frequency domain with equidistant spacing of the spectral lines, as shown in Fig. 1d. The periodic bursting behavior in amplitude results from a relative phase slip between the modal responses and the driving signal. This type of phase slip is similar to classic examples like the damped, driven pendulum and the Josephson junction near critical current (see Strogatz [31] Ch. 4 and 8), with a more interesting response near the bursts due to additional degrees of freedom resulting from the coupled resonant modes.

To explain these results, we introduce the non-dimensional Hamiltonian describing the mode coupling through a nonlinear 1 : 3 internal resonance. The two vibrational modes are characterized by coordinates q_k and momenta p_k ($k = 1, 2$). The primary mode ($k = 1$) is subjected to harmonic drive and has a Duffing nonlinearity.

$$\begin{gathered} H = H_1 + H_2 + H_{int} + H_F, \\ H_1 = \frac{1}{2}p_1^2 + \frac{1}{2}\omega_{01}^2 q_1^2 + \frac{1}{6}\omega_1 q_1^4, \;\; H_2 = \frac{1}{2}p_2^2 + \frac{1}{2}\omega_{02}^2 q_2^2, \\ H_{int} = \frac{2}{3}\omega_1 \kappa q_1^3 q_2, \quad H_F = -4\omega_1 q_1 F\cos(\omega_1 t), \end{gathered} \tag{1}$$

where ω_{0i} are the modal natural frequencies, κ is the inter-modal coupling strength, and $F \propto V_{\rm o}$ is the strength of an external periodic field that drives the primary mode at the angular frequency, ω_1. The explanation of the conversion to the non-dimensional parameters can be found in the supplemental materials. In our analysis, we also assume that both modes are coupled to a thermal reservoir, leading to corresponding linear friction forces $-2\Gamma_{1,2}\dot{q}_{1,2}$. The values for the modal parameters are determined from standard experimental measurements of the two individual modes separately as described in supplemental materials while the value of the coupling, κ, is obtained by matching the experimental coupled mode response of the device to predictions from the model.

By grouping the terms of the second mode in Eq. 1, it is seen that the response of the second mode is that of a simple harmonic oscillator being resonantly driven by the motion of the first vibrational mode. Once excited, the amplitude of the second mode results in back-action on the dynamics of the first mode, dictated by the normalized coupling coefficient, κ. Also, note that the interaction between the two modes is described by a single term that is sufficient to capture the features of the resonance through the normal form for this resonance [29]. Importantly, this form of the inter-modal coupling arises naturally due to an asymmetry in the equations of motion for flexural and torsional degrees of freedom and their intrinsic nonlinearities [21]. As a result, the linear modal (eigen-) coordinates, $q_{\rm i}$, correspond to vibrational modes that are primarily dominated by the flexural and torsional motions, respectively, but are combinations of these degrees of freedom.

In order to understand the dynamics of the system observed experimentally and described by the model in Eq. 1 with linear friction forces, it is convenient to switch to the rotating frame of reference by transforming q_i to their complex amplitude form (Supplemental Materials). This yields the following system of equations for normalized complex mode amplitudes A_1 and A_2:

$$\dot{A}_1 = -[1 + i(\Delta\omega_1 - |A_1|^2)]A_1 + i\kappa A_2 \bar{A}_1^2 - iF, \tag{2}$$

$$\dot{A}_2 = -(\Gamma_{21} + i\Delta\omega_2)A_2 + \frac{i\kappa}{9}A_1^3. \tag{3}$$

where $\Delta\omega_1 = 2\pi(f_{\rm F} - f_{\rm flex})/\Gamma_1$, $\Delta\omega_2 = 2\pi(3f_{\rm F} - f_{\rm tor})/\Gamma_1$, and $\Gamma_{21} = \Gamma_2/\Gamma_1$. This model provides a means of pre-

dicting the system response as drive parameters (F and f_F) are varied. The steady state response (A_{1s}, A_{2s}) of the coupled system can be found by solving $\dot{A}_i = 0$, yielding an implicit expression for the A_{1s} in terms of the system and drive parameters (Supplemental Materials),

$$F = i\left[1 + i(\Delta\omega_1 - |A_{1s}|^2) + \frac{\kappa^2 |A_{1s}|^4}{9(\Gamma_{21} + i\Delta\omega_2)}\right] A_{1s}. \quad (4)$$

From Eq. 3 and Eq. 4, it is seen that the coupling becomes important when $|\Delta\omega_2| \approx \Gamma_{21}$. Of interest here are SN bifurcation conditions of the steady-state, which correspond to the merging and annihilation of pairs of responses. For example, at the edges of bi-stability in the Duffing model, these bifurcations can be found from conditions for degenerate (repeated) solutions of Eq. 4. From the model, the bifurcations occur at the solid blue line in Fig. 2a. In the coupled system, when mode A_1 is excited with relatively strong drive and the drive frequency is increased, at the frequency, f_{SN}, a SN bifurcation occurs before the Duffing SN, due to the resonant interaction with the torsional mode. The SN condition saturates near $f_{\mathrm{tor}}/3$ (Fig. 2(a) red line). When overlaid with the experimental data (black circles), Fig. 2a, the predictive model agrees with and fits the data very well considering the complex behavior of two coupled modes. Additional comparison between the model and the experimental data can be found in the supplemental materials with references [32] [33].

The manner in which the SN bifurcation creates the long period response shown in Fig. 1 can be qualitatively explained using the stability graphics shown in Figs. 2 (b)-(d) (top: 1D case; bottom: 2D case). When the resonator is driven at a frequency slightly less than f_{SN} (Fig. 2b), a stable operating point exists, represented by the solid black circles in both the 1D and the 2D cases. The open circles represent operating points that are dynamically unstable. As the drive frequency is increased and reaches f_{SN}, the system dynamic undergoes a SN bifurcation (Fig. 2c) where the stable and unstable solutions merge to form a degenerate saddle node in 1D, and a SN on an invariant circle (SNIC) in 2D. As the drive frequency is increased beyond f_{SN} (Fig. 2d), the response moves away from the SNIC bifurcation, and no stable solution exist. However, the dynamic of the system is still influenced by the proximity to the SNIC bifurcation. In the 1D case, it results in a range of operating values where the system dynamics slow down as represented by smaller arrows in the stability diagram. In 2D, there are no steady operating points on the limit cycle, as a consequence, the resonator simply circles the limit cycle indefinitely. However, the remnant of the SN bifurcation (not easily visualized in 2D) affects the local time scales. This is schematically shown by slow flow (small arrows) and fast flow (large arrows) as the resonator traverses the limit cycle. Mathematically this can be described by two time parameters, τ_1 and τ_2. τ_1 represents the length of the response burst and τ_2 represents the strength of the remnant, which varies strongest with the coupling parameter, κ. This bifurcation structure dictates a scaling law for the period of the limit cycle near the SNIC bifurcation, which is dominated by the slow part of the cycle and is given by [31]:

$$T = \tau_1 + \tau_2 (f_{\mathrm{F}} - f_{\mathrm{SN}})^{-1/2} \quad (5)$$

where T is the period of the cycle, τ_1 is the duration of the fast burst, τ_2 accounts for the slow dynamics near the remnant of the SN, and $f_{\mathrm{F}} - f_{\mathrm{SN}}$ is the detuning of the frequency from the SNIC bifurcation. As the driving frequency is further increased, the remnant of the bifurcation becomes weaker, reducing the influence of the SNIC, and the period of the limit cycle approaches τ_1.

The observed modulated amplitude behavior of the resonator near the SNIC bifurcation is characterized by fixing the drive amplitude and measuring the temporal response of the resonator for various drive frequencies moving across f_{SN} (Fig. 2a green line). For frequencies less than f_{SN}, the response of each mode as a function of time is constant because the resonator operates at a stable point (Fig. 2b). As the frequency is increased greater than f_{SN}, the magnitudes of the responses of the two modes transition abruptly from constant to a periodic modulation, as expected from the SNIC bifurcation. The response of a single cycle shows a period of time spent near the SN remnant (τ_1) followed by an excursion (burst) (τ_2) until the response again approaches the SN remnant. As the frequency is further increased, the resonator continues with a periodic modulated response with bursting periods becoming shorter as the remnant of the SN becomes weaker. Fig. 3a and 3b show plots of single period responses as the frequency is increased from f_{SN} (blue, black), demonstrating the change in the temporal response to f_{SN}.

The spectral responses (fast Fourier Transform) of the time data, for a time period of 40s of the bursting behaviors are shown in Fig. 3c as a function of the frequency detuning, $f_F - f_{\mathrm{SN}}$. Only the fundamental frequency and the first comb frequency are shown for clarity. The center frequencies of the different drives are shifted to zero to clearly show the change in comb spacing as the frequency offset is increased. Finally, Fig. 3d shows a plot of the period as the frequency is detuned from f_{SN}. Fitting this to Eq. 5, we obtain a very good match with a value of 0.32 s for τ_1 and 0.47 $s^{1/2}$ for τ_2. This demonstrates tunability of the length of the time excursions and concurrently the spacing of the frequency combs by a single parameter, the frequency offset from the SNIC bifurcation. By controlling the drive frequency, the spacing of the combs in the frequency spectra is completely determined. The understanding of the bifurcation structure provides the necessary mathematical basis to predict the response of the system. Additionally, since the normal

form for this internal resonance is generic [29], this behavior is not limited to only this mechanical resonator but applicable to vastly different systems that follow this normal form with comparable parameter conditions.

In summary, we demonstrate the first experimental realization of a SNIC bifurcation in a mechanical device. It results in a temporal response with bursting behavior separated by periods of near steady response and whose attendant frequency response shows a "frequency comb" spanning a bandwidth of about two orders of magnitude larger than the linear dissipation rate. The experimental results are accurately captured by a dynamical model for 1:3 internal resonance with parameters determined from the experimental device. The parameters obtained for the model and general knowledge about the nature of this response allow us to accurately predict the influence of drive parameters on the spacing of the frequency comb. The generic nature of the model for this internal resonance indicates that similar dynamic behaviors and bifurcation structures will occur for systems exhibiting this internal resonance, regardless of the physical nature of the system. For example, many biological systems exhibit behaviors that change with environmental stimuli that can be described by bifurcations [34], specifically, the SNIC bifurcation has been proposed as a model for neuron spiking [13], potentially opening up new ways to emulate neuron interactions [35] through completely mechanical and easily controlled systems.

The authors would like to acknowledge Mark Dykman for helpful discussion regarding both the theoretical and experimental results. This work was performed, in part, at the Center for Nanoscale Materials, a U.S. Department of Energy Office of Science User Facility, and supported by the U.S. Department of Energy, Office of Science, under Contract No. DE-AC02-06CH11357. OS acknowledges partial support from Ben-Gurion University of the Negev. AME acknowledges support from the Swedish Research Council (VR). SWS acknowledges support for this work from the US National Science Foundation under grants CMMI-1662619 and CMMI-1561829.

* dczaplewski-at-anl.gov

[1] R. De Alba, F. Massel, I. Storch, T. Abhilash, A. Hui, P. McEuen, H. Craighead, and J. Parpia, Nature Nanotechnology **11**, 741 (2016).
[2] I. Mahboob, E. Flurin, K. Nishiguchi, A. Fujiwara, and H. Yamaguchi, Nature communications **2**, 198 (2011).
[3] J. Güttinger, A. Noury, P. Weber, A. M. Eriksson, C. Lagoin, J. Moser, C. Eichler, A. Wallraff, A. Isacsson, and A. Bachtold, Nature nanotechnology **12**, 631 (2017).
[4] F. Sun, X. Dong, J. Zou, M. I. Dykman, and H. Chan, Nature communications **7** (2016).
[5] A. Shkarin, N. Flowers-Jacobs, S. Hoch, A. Kashkanova, C. Deutsch, J. Reichel, and J. Harris, Physical Review Letters **112**, 013602 (2014).
[6] P. Del'Haye, A. Coillet, T. Fortier, K. Beha, D. C. Cole, K. Y. Yang, H. Lee, K. J. Vahala, S. B. Papp, and S. A. Diddams, Nature Photonics (2016).
[7] O. Shoshani, S. Shaw, and M. Dykman, Scientific reports **7**, 18091 (2017).
[8] E. Verhagen, S. Deléglise, S. Weis, A. Schliesser, and T. J. Kippenberg, Nature **482**, 63 (2012).
[9] H. Okamoto, A. Gourgout, C.-Y. Chang, K. Onomitsu, I. Mahboob, E. Y. Chang, and H. Yamaguchi, Nature Physics **9**, 480 (2013).
[10] I. Mahboob, H. Okamoto, and H. Yamaguchi, Science Advances **2**, e1600236 (2016).
[11] T. Faust, J. Rieger, M. J. Seitner, J. P. Kotthaus, and E. M. Weig, Nature Physics **9**, 485 (2013).
[12] G. Buzsáki and A. Draguhn, science **304**, 1926 (2004).
[13] M. Kantner, E. Schöll, and S. Yanchuk, Scientific reports **5** (2015).
[14] J. P. Mathew, R. N. Patel, A. Borah, R. Vijay, and M. M. Deshmukh, Nature nanotechnology (2016).
[15] W. G. Conley, A. Raman, C. M. Krousgrill, and S. Mohammadi, Nano letters **8**, 1590 (2008).
[16] R. Karabalin, M. Cross, and M. Roukes, Physical Review B **79**, 165309 (2009).
[17] S. H. Nitzan, V. Zega, M. Li, C. H. Ahn, A. Corigliano, T. W. Kenny, and D. A. Horsley, Scientific reports **5**, 9036 (2015).
[18] I. Mahboob, R. Dupuy, K. Nishiguchi, A. Fujiwara, and H. Yamaguchi, Applied Physics Letters **109**, 073101 (2016).
[19] G. Arioli and F. Gazzola, Applied Mathematical Modelling **39**, 901 (2015).
[20] D. Antonio, D. H. Zanette, and D. López, Nature communications **3**, 806 (2012).
[21] C. Chen, D. H. Zanette, D. A. Czaplewski, S. Shaw, and D. López, Nature communications **8**, 15523 (2017).
[22] K. Qalandar, B. Strachan, B. Gibson, M. Sharma, A. Ma, S. Shaw, and K. Turner, Applied Physics Letters **105**, 244103 (2014).
[23] I. Mahboob, Q. Wilmart, K. Nishiguchi, A. Fujiwara, and H. Yamaguchi, Applied Physics Letters **100**, 113109 (2012).
[24] L. Cao, D. Qi, R. Peng, M. Wang, and P. Schmelcher, Physical review letters **112**, 075505 (2014).
[25] M. J. Seitner, M. Abdi, A. Ridolfo, M. J. Hartmann, and E. M. Weig, Physical Review Letters **118**, 254301 (2017).
[26] A. Ganesan, C. Do, and A. Seshia, Physical review letters **118**, 033903 (2017).
[27] A. Ganesan, C. Do, and A. Seshia, Applied Physics Letters **112**, 021906 (2018).
[28] D. Antonio, D. A. Czaplewski, J. Guest, D. López, S. Arroyo, and D. H. Zanette, Physical Review Letters **114**, 034103 (2015).
[29] J. Guckenheimer and P. J. Holmes, *Nonlinear oscillations, dynamical systems, and bifurcations of vector fields*, Vol. 42 (Springer Science & Business Media, 2013).
[30] R. Mestrom, R. Fey, J. Van Beek, K. Phan, and H. Nijmeijer, Sensors and Actuators A: Physical **142**, 306 (2008).
[31] S. H. Strogatz, *Nonlinear dynamics and chaos: with applications to physics, biology, chemistry, and engineering* (Hachette UK, 2014).
[32] P. Bergé, Y. Pomeau, and C. Vidal, *Order within chaos* (Wiley and Sons NY, 1984).

[33] G. Bachar, E. Segev, O. Shtempluck, S. W. Shaw, and E. Buks, EPL (Europhysics Letters) **89**, 17003 (2010).
[34] Y. Murayama, H. Kori, C. Oshima, T. Kondo, H. Iwasaki, and H. Ito, Proceedings of the National Academy of Sciences **114**, 5641 (2017).
[35] E. M. Izhikevich, *Dynamical systems in neuroscience* (MIT press, 2007).

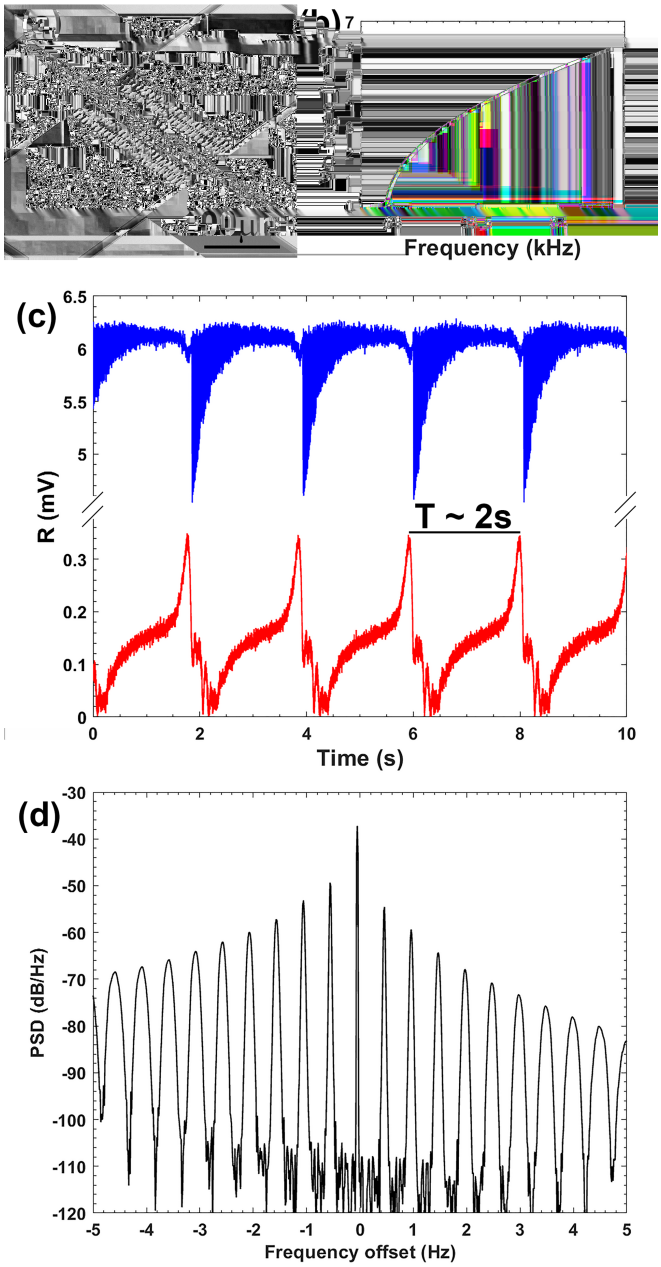

FIG. 1. Nonlinear microelectromechanical resonator with bursting response. (a) SEM of the microelectromechanical resonator with a scale bar of 100 μm. (b) Amplitude response curves of the resonator as a function of drive frequency, f_{F}, for different drive voltages, V_{o}, (mV): 2 (gray), 5 (red), 10 (blue), 15 (purple), 17 (black). (c) Temporal amplitude response of the flexural (blue) and torsional (red) responses showing the bursting behavior. (d) Frequency spectrum of the temporal response measured in (c) showing the generation of a frequency comb.

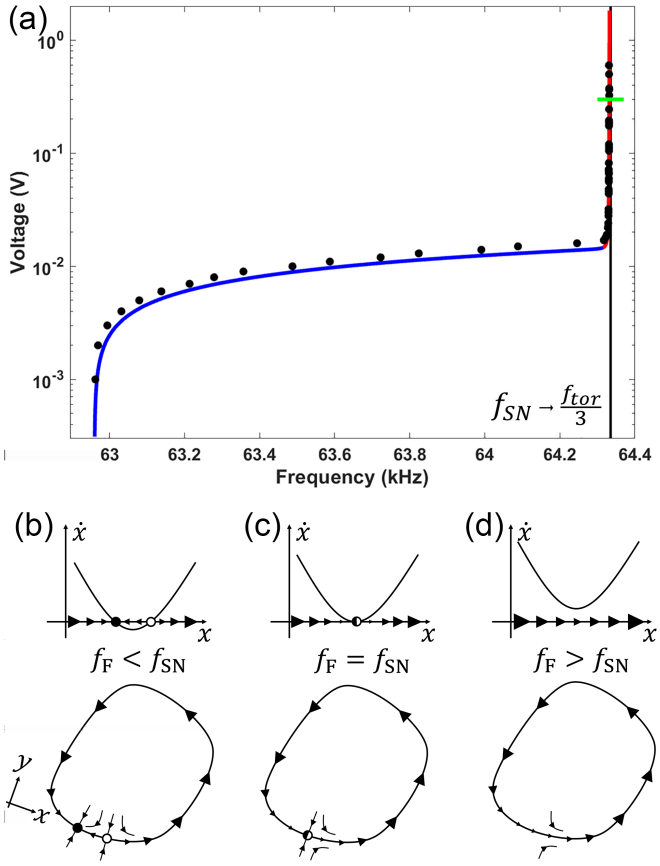

FIG. 2. (a) Theoretical (colored lines) and experimental (black circles) SN bifurcation conditions in the $(Voltage, f_F)$ parameter plane. The solid blue line shows the SN bifurcations resulting from Duffing while the red line shows the SN saturation near $f_{tor}/3$. (b), (c), (d) Schematic of the SNIC bifurcation structures for the resonator near internal resonance, indicating the slow 1D dynamics (top row, local to the SN bifurcation) and the global setting with the cycle connection, depicted here in 2D (bottom row, showing a higher dimensional response with the IC). The black solid circles (stable) and hollow circles (unstable) represent steady-state operating points. Large (small) arrows indicate fast (slow) dynamics. As the frequency is increased from below to above f_{SN}, the steady-state branches merge and disappear, leaving the system to perform periodic motion on the invariant cycle.

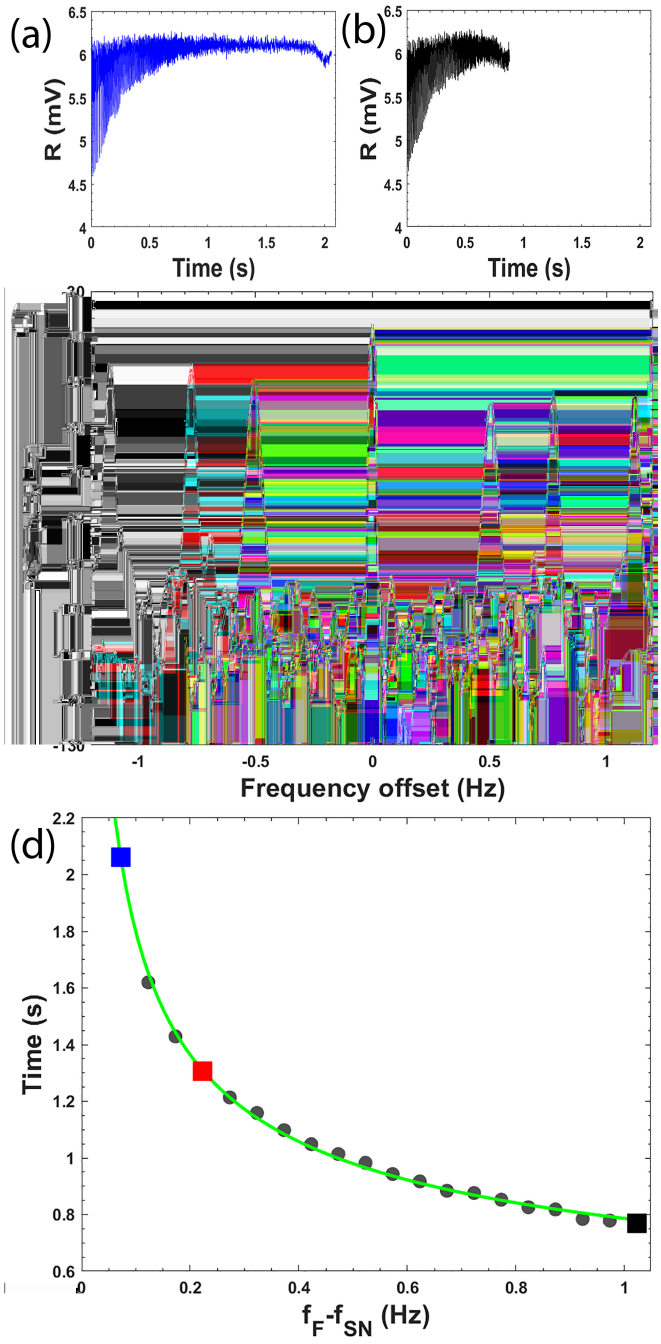

FIG. 3. Experimental control of the SNIC period and corresponding frequency combs. (a) Single period of the temporal response of the resonator as the drive frequency is increased from f_{SN} by 0.07 Hz. (b) Single period of the temporal response of the resonator as the drive frequency is increased from f_{SN} by 1.02 Hz. (c) Spectral response of the resonator for frequency offsets from f_{SN} of 0.07 HZ, 0.22 Hz and 1.02 Hz, showing increased spacing of the comb frequencies, corresponding to the temporal plots in (a) and (b). (d) Period of response as a function of frequency offset (gray circles and the three cases in (c) shown as blue, red and black squares) and a least-squares fit (green line) to the theoretical scaling (Eq. 5) of the period, T, near the SNIC bifurcation.